Electronic Supplementary Material (ESI) for Inorganic Chemistry Frontiers.

Supporting Information

Promoting Oxygen Reduction via Crafting Bridge-bonded Oxygen Ligands on Iron Single-Atom Catalyst

Chuanlan Xu[a,b], Yujun Si[c], Bingbing Hu[d], Xinru Xu[b], Bihao Hu[a], Ying Jiang[b], Haifeng Chen[b], Chaozhong Guo[a,b]*, Honglin Li[e]**, Changguo Chen[a]***

[a]*College of Chemistry and Chemical Engineering, Chongqing University, Chongqing 401331, China.*

[b]*Chongqing Key Laboratory of Materials Surface & Interface Science, Chongqing University of Arts and Sciences, Chongqing 402160, China.*

[c]*College of Chemistry and Environmental Engineering, Sichuan University of Science and Engineering, Zigong 643000, China*

[d]*College of Materials Science and Engineering, Chongqing Jiaotong University, Chongqing, 400074, China.*

[e]*College of Physics and Electronic Engineering, Chongqing Normal University, Chongqing, 401331, China.*

** Corresponding authors.*

E-mail addresses*: guochaozhong1987@163.com (C. Guo); 172093818@163.com (H. Li); cgchen@cqu.edu.cn (C. Chen)*

Experimental

Chemical reagents and materials:

$FeCl_3 \cdot 6H_2O$ was obtained from Shanghai Macklin Biochemical Co., Ltd. Dopamine hydrochloride, and iron phthalocyanine were obtained from Aladdin®. Nafion (5 wt%) was obtained from Shanghai Hesen Electric Co. Ltd. Pt/C (20 wt%) was obtained from Alfa Aesar. All other chemical reagents were from Chengdu Kelong Chemical Co., Ltd and used as received without further purification. Milli-Q ultrapure water was used for all experiments with a resistivity of 18.25 $M\Omega\ cm^{-1}$.

Characterizations and methods:

Scanning electron microscopy (SEM) measurements were performed with Gemini, SEM-300 field emission scanning electron microscope. Transmission electron microscopy (TEM), high resolution transmission electron microscopy (HRTEM), high-annular dark-field scanning transmission electron microscopy (STEM) and element mapping analysis were conducted on FEI Talos F200X electron microscope operating at 200 kV. The Atomic-resolution HAADF/STEM images and electron diffraction patterns were performed on a FEI Titan Themis Z microscope equipped with a probe-forming aberration corrector and operated at 300 kV. Atomic force microscopy (AFM) was conducted on Dimension Icon (Bruker, USA) with a force constant of ~ 48 N/m and scanning rate of 1.0 Hz. X-ray diffractometer (XRD) was tested on Shimadzu XRD6000 with Cu Kα radiation at 30 kV. Raman measurements were recorded on an Invia/Reflrx Lasser Micro-Raman spectroscope (Renishaw, England) with excitation laser beam wavelength of 532 nm. Specific surface areas and pore size distributions were determined from nitrogen sorption isotherms collected at 77 K on ASAP 2460 apparatus (micromeritics, USA). X-ray photoelectron spectra (XPS) were determined by an X-ray photoelectron spectrometer (Thermo escalab 250Xi, Thermofisher, USA). The X-ray absorption spectra (XAS) including X-ray absorption near-edge structure (XANES)and extended X-ray absorption fine structure (EXAFS)of the samples at Fe K-edge (7709eV were collected at the Singapore Synchrotron Light Source (SSLS) center, where a pair of channel-cut Si (111) crystals was used in the monochromator. The acquired EXAFS data were extracted and processed according to the standard procedures using the ATHENA module implemented in the FEFIT software packages.

Experimental section:

Synthesis of 2D porous carbon nanosheets: The 2D porous carbon nanosheets were first synthesized and prepared with a salt-templating polymerization method combined with freeze-drying and pyrolyzing. Typically, 2.0 g of $FeCl_3 \cdot 6H_2O$ was added into 5.0 mL of deionized water (A), while 0.20 g of dopamine hydrochloride was dissolved in another 2.0 mL of deionized water (B). B was dropwise added into A with constant stirring and aged overnight. After freeze-drying, the black powder was immediately pyrolyzed at 700, 800, and 900 °C for 120 min with a ramp rate of 5 °C/min under an Ar atmosphere. The resulting powder was etched with 0.5 M H_2SO_4 to eliminate the excess iron salt and washed to neutral. Subsequently, the obtained materials were dried at 60 °C overnight. The secondary thermal treatment of our catalysts was performed at the corresponding temperature under an Ar atmosphere for 2 h, and the products heated at 700, 800, and 900 °C were named Fe/N-G-700, Fe/N-G-800, and Fe/N-G-900, respectively.

For comparison, a series of Fe/N-G-800 composites were also prepared via the same procedure except that the mass feed ratio of dopamine hydrochloride to $FeCl_3 \cdot 6H_2O$ was changed to 1:5, 1:10, and 1:20, respectively.

Synthesis of Fe@Fe/N-G-800: The obtained Fe/N-G-800 (25 mg) was added to 60 mL of DMF solution containing 5 mg of FePc. To get the uniform suspension, the mixture solution was subjected to ultrasonic treatment for 1h and then stirred overnight at room temperature. Finally, the Fe@Fe/N-G-800 composite was collected by filtration of the resulting solution and washing with ethanol. The obtained sample was dried in a vacuum at 60 °C for 12 h.

Synthesis of Fe/N-G-800/FePc: The Fe/N-G-800/FePc were obtained by the direct physical mixture of FePc with the Fe/N-G-800. The as-obtained Fe/N-G-800 (25 mg) and 5 mg of FePc were mixed by simple grinding.

Synthesis of CB-FePc and OCB-FePc: Here, the Hummers method was used to oxidatively modify the surface of carbon black (CB) to obtain O-containing carbon black (OCB). The CB or OCB (25 mg) was added to 60 mL of DMF solution containing 5 mg of FePc. To get the uniform suspension, the mixture solution was subjected to ultrasonic treatment for 1h and then stirred overnight at room temperature. Finally, the CB-FePc or OCB-FePc composite was collected by filtration of the resulting solution and washing with ethanol. The obtained sample was dried in a vacuum at 60 °C for 12 h.

Electrochemical measurements:

All the electrochemical measurements were carried out in a conventional three-electrode cell using the PINE electrochemical workstation (Pine Research Instrumentation, USA) and a CHI 760E electrochemical workstation (CH Instruments, Chenhua Co., China) at room temperature, with a graphite rod as the counter electrode, a Hg/HgO as the reference electrode, and a glassy carbon rotating ring-disk electrode (RRDE) (Φ = 5.6 mm) as the working electrode. The catalyst ink was prepared by adding 1 mg of a catalyst into a solution containing water, isopropanol, and Nafion (5%) at a volume ratio of 16:1:1 to form a homogeneous suspension at the catalyst concentration of 5 mg mL^{-1}. A calculated amount (19 μL) of the suspension was then evenly cast on the clean RRDE surface with a syringe and dried in the air, corresponding to a catalyst loading of 0.384 mg cm^{-2}. The electrolyte was 0.1 M KOH solution. RRDE measurements were conducted by linear sweep voltammetry (LSV) from 1.1 V to 0 V at a scan rate of 10 mV s^{-1} at 1600rpm, while the ring electrode was held at 1.5 V vs. RHE. The accelerated durability tests (ADTs) were carried out in O_2 -saturated 0.1 M KOH solution in the potential range from 0.6 to 1.0 V at the scan rate of 100 mV s^{-1}. All the potentials were converted to values versus the reversible hydrogen electrode (RHE) according to the Nernst equation ($V_{RHE} = V_{Hg/HgO} + 0.0591$ pH + 0.098).

The four-electron selectivity of catalysts was evaluated based on the H_2O_2 yield, calculated from the following equation (1):

$$H_2O_2(\%) = 200 \times \frac{I_R/N}{(I_R/N)+I_D} \qquad (1)$$

The electron transfer number can be calculated based on the following equation (2):

$$n = 4 \times \frac{I_D}{(I_R/N)+I_D} \qquad (2)$$

Here, I_D and I_R are the disk and ring currents, respectively, and N = 0.38 is the ring collection efficiency.

Electrochemical capacitance was determined using CV measurements. First, the potential range of non-faradaic current response was determined by CV in 1 M KOH solution. The range is typically a 0.1 V window centered at the open circuit potential (OCP) of the system. Secondly, CV was conducted at different scan rates (0.002-0.014 V s^{-1}) to evaluate the electrochemical double-layer capacitance (C_{dl}). The charging current, i_c, is then measured from CVs at multiple scan rates. The double-layer charging current is equal to the product of the scan rate, v, and the electrochemical double-layer capacitance, C_{dl}, as given by eq:

$$i_c = v\, C_{dl} \quad (3)$$

Therefore, a plot of i_c as a function of v yields a straight line with a slope equal to C_{dl}.

Zn-air Battery Measurements:

The Zinc-Air battery test was carried out using a home-made Zn–O_2 battery in a 6 M KOH solution, and pure oxygen was used as cathode reactant. Both the loading of Fe@Fe/N-G-800 and commercial Pt/C (20%) are 0.5 mg cm^{-2}. The catalysts ink was prepared by dispersing 2 mg catalysts in 195μL alcohol and 5 μL nafion (5 wt.%) solution. Then the catalysts ink was uniformly coated onto the carbon paper and dried at room temperature. A Zn plate and the carbon paper with catalysts were used as the anode and cathode respectively. A piece of nickel foam was used as the current collector. Both electrodes and the current collector were assembled into the Zn-O_2 battery. The polarization curves were recorded by linear sweep voltammetry (LSV) at a sweep rate of 10 mV s^{-1}.

Computational methods:

In this work, the initial models of different structures were built using VESTA.[1] First-principles calculations are performed by using the DFT approach as implemented in the Vienna Ab initio Simulation Package (VASP) code with the projector-augmented-wave (PAW) method. [2-6] For the exchange and correlation energies, the generalized gradient approximation (GGA) in the form of Perdew-Burke-Ernzerhof (PBE) functional is adopted.[7] Considering the reality that the vdW interaction has an unneglected effect on the final stability of the heterostructures, the standard PBE function cannot handle this weak interaction well, so we adopted the DFT-D2 method by Grimme to describe the weak vdW interaction between two layers in all calculations, [8] in which all the force field parameters are obtained based on the PBE function. The total energy (E_{total}) is expressed as: $E_{total} = E_{KS}\text{-}DFT + E_{vdW}$, where $E_{KS}\text{-}DFT$ and E_{vdW} are Kohn-Sham DFT energy and dispersion correction respectively. [9, 10] The first Brillouin-zone sampling of 1×1×1 and 3×3×1 k-points generated by Monkhorst-Pack scheme are used for geometric optimization/molecular dynamics and energy calculations, respectively. The vacuum layer is set to 20 Å along the Z direction to avoid the interactions induced by the periodic effects. To find a balance between accuracy and efficiency, a 500 eV cut-off energy has been adopted in all calculations. The pristine and heterojunction structures were optimized until the forces on each atom are less than 10^{-4} eV and the Hellmann-Feynman force on each atom is 0.01 eV $Å^{-1}$, which was sufficient enough to reach convergence for the whole calculations. The charge density different is obtained by: $\Delta\rho = \rho^{AB} - \rho^{A} - \rho^{B}$.

The free energies of reactants and each intermediate state at an applied electrode potential U were calculated as follows: $\Delta G = \Delta E + \Delta ZPE - T\Delta S - neU$, where n is the electron number of such state and ΔE represents the change in enthalpy which is considered from the DFT total energy value, ΔZPE represents the change in zero-point energy and ΔS represents the change in entropy. Since it is difficult to obtain the exact free energy of OOH, O, and OH radicals in the electrolyte solution, the adsorption free energy ΔG_{OOH*}, ΔG_{O*}, and ΔG_{OH*} are used in the calculations. The equilibrium potential U_0 for ORR at pH = 13 was determined to be 0.455 V vs. NHE where the reactant and product are at the same energy level. The free energy of $H_2O(l)$ was derived as $G_{H2O(l)} = G_{H2O(g)} + RT*\ln(p/p_0)$ since only $G_{H2O(g)}$ can be directly obtained by DFT calculations. The free energy of $O_2(g)$ was derived as $G_{O2(g)} = 2G_{H2O(l)} - 2G_{H2} - 4.92$ eV. [11] The free energy of OH^- was derived as $G_{OH-} = G_{H2O(l)} - G_{H+}$, where $G_{H+} = 1/2G_{H2} - k_BT\ln 10 * pH$. The overall reaction scheme of ORR in alkaline environment is: $O_2 + 2H_2O + 4e^- \rightarrow 4OH^-$, [12] and the following associative mechanism is considered in our calculations:

$$O_2(g) + * + H_2O + e^- \leftrightharpoons *OOH + OH^- \quad (1)$$

$$*OOH + e^- \leftrightharpoons *O + OH^- \quad (2)$$

$$*O + H_2O + e^- \leftrightharpoons *OH + OH^- \quad (3)$$

$$^{*}OH + e^{-} \leftrightarrows {}^{*} + OH^{-} \qquad (4)$$

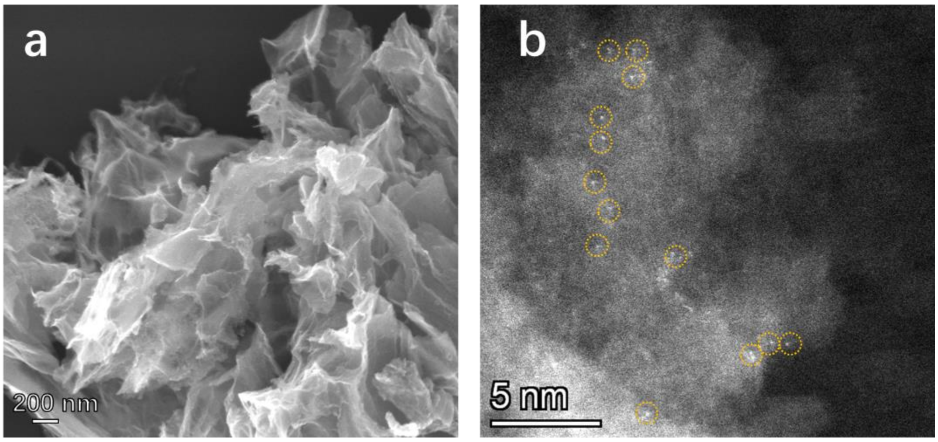

Figure S1. a) SEM image of Fe/N-G-800, b) aberration-corrected HAADF-STEM of the isolated Fe atoms involved Fe/N-G-800 catalyst.

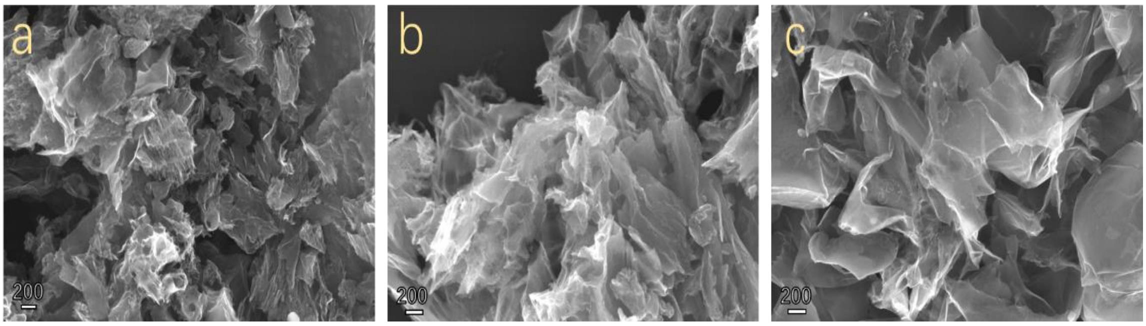

Figure S2. SEM images of DA/$FeCl_3$ with an initial mass ratio of a) 1:5, b) 1:10, and c) 1:20.

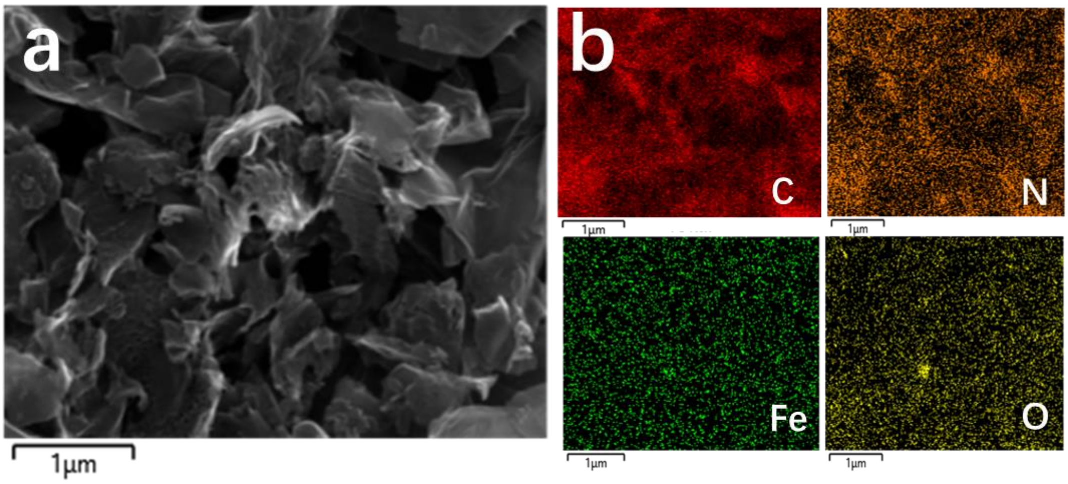

Figure S3. a) SEM image of Fe/N-G-800/FePc, b) EDS mapping (C red,N orange, Fe green, O yellow)

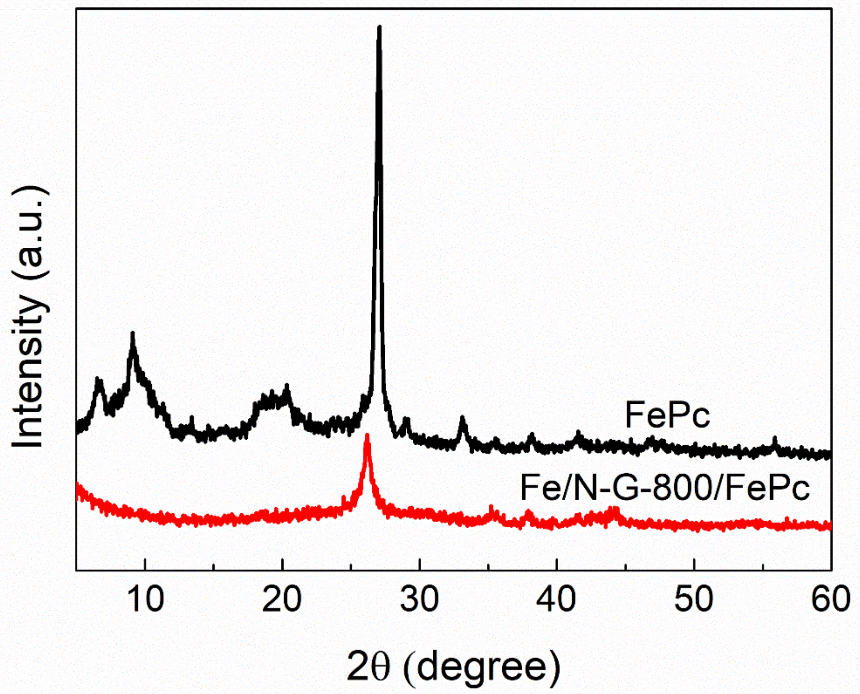

Figure S4. XRD patterns of FePc and Fe/N-G-800/FePc.

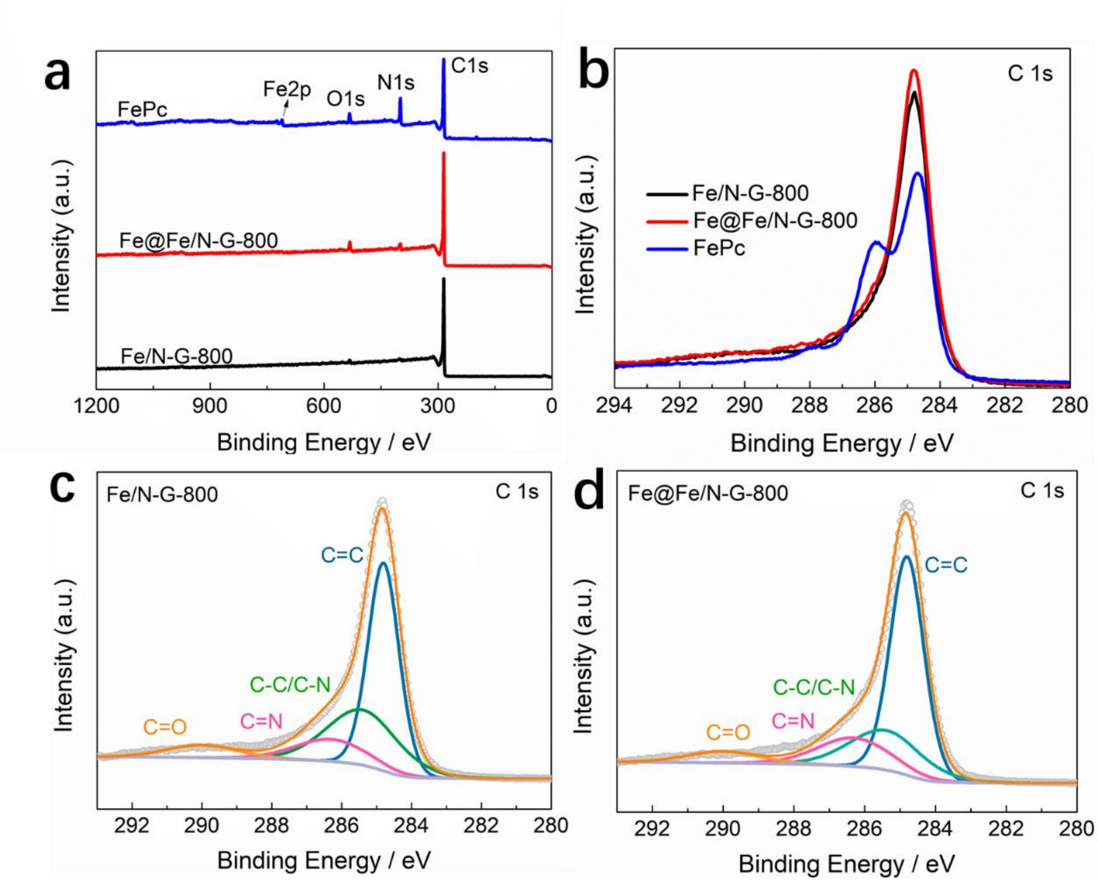

Figure S5. a) XPS survey and b) C 1s XPS of various catalysts. High resolution C 1s XPS for c) Fe/N-G-800 and d) Fe@Fe/N-G-800.

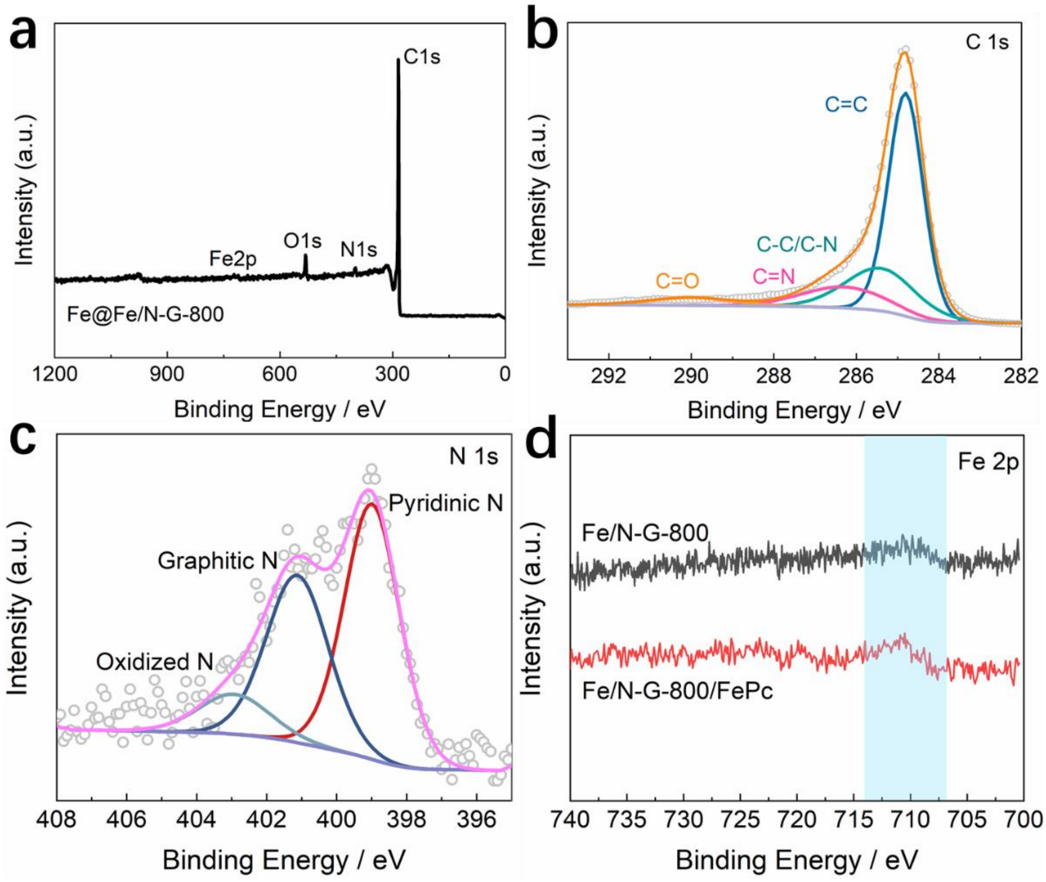

Figure S6. a) XPS survey; b) high resolution XPS of C 1s, c) N 1s, and d) Fe 2p for Fe/N-G-800/FePc and Fe/N-G-800.

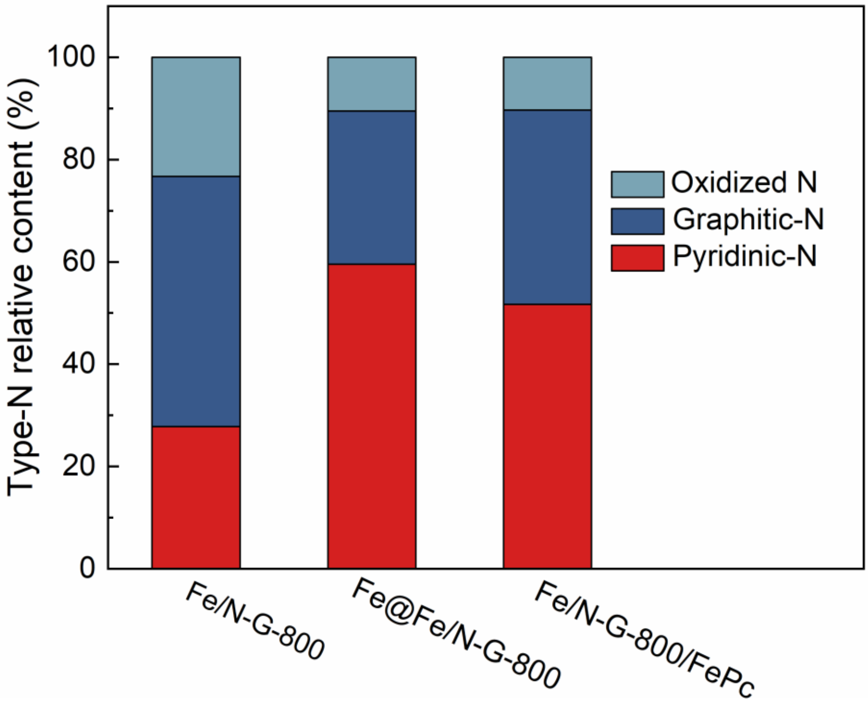

Figure S7. Relative ratio of N content of various catalysts.

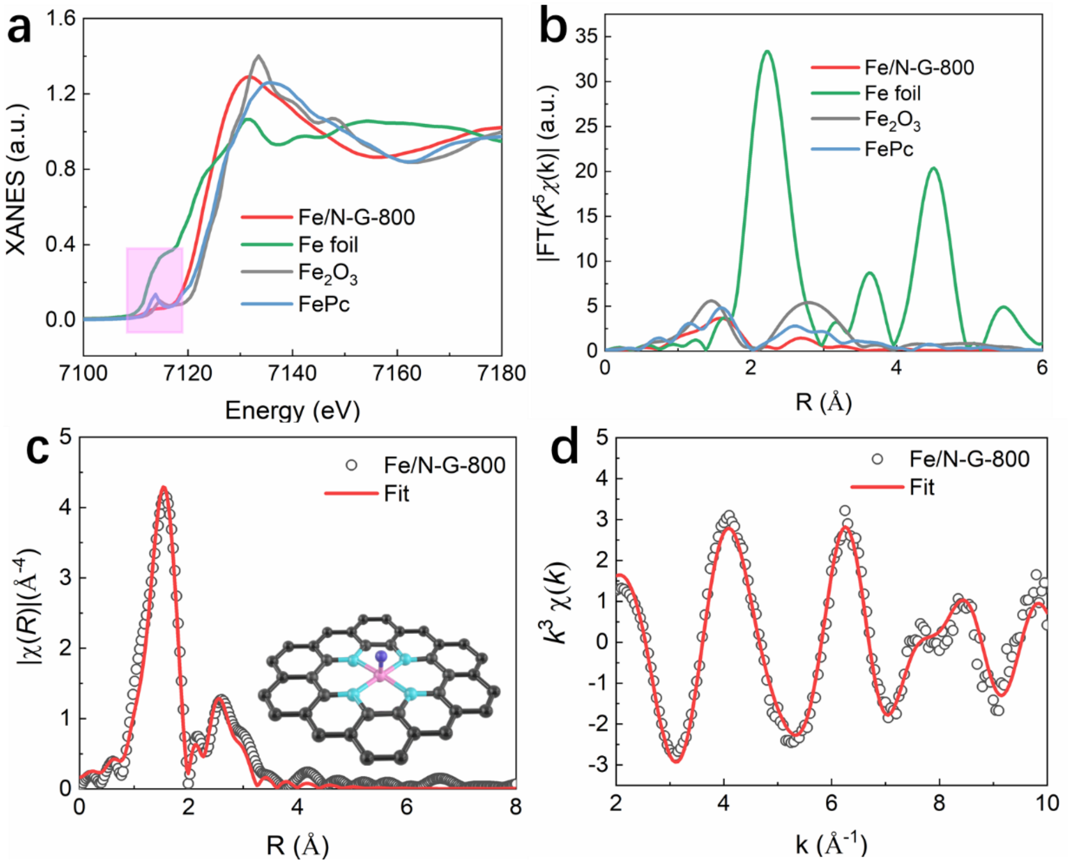

Figure S8. a) XANES at the Fe K-edge and b) FT-EXAFS spectra of the Fe foil, Fe_2O_3, FePc, and Fe/N-G-800 in R space; c) Comparison between experimental and fitting results of the FT-EXAFS of Fe/N-G-800 in R space; d) Comparison between experimental and fitting results of the FT-EXAFS of Fe/N-G-800 in k space.

Figure S8 shows the Fe K-edge X-ray absorption near-edge structure (XANES) spectra of Fe/N-G-800, Fe foil, Fe_2O_3, and FePc. The pre-edge at 7113 eV of Fe/N-G-800 suggests the deviation of Fe-N_4 squareness and the existence of an axial ligand. [13] The absorption threshold position of Fe/N-G-800 is located between FePc and Fe_2O_3, indicating that the valence state of the Fe atom in Fe/N-G-800 is situated between +2 (FePc) and +3 (Fe_2O_3).[14] The coordination configuration of isolated Fe atoms in Fe/N-G-800 was investigated by extended X-ray absorption fine structure

(EXAFS). The peak at ~1.59 Å in R space of Fourier-transformed (FT) k^3-weighted Fe K-edge EXAFS is assigned to the Fe-N scattering path (Figure S10c). The EXAFS fitting results show that the coordination numbers of Fe-N and Fe-O are 3.8 and 1.0, respectively, and the average bond distance is 2.05 Å (Table S3). Based on the above results, it is reasonable that the coordination structure of Fe in Fe/N-G-800 is FeN_4O.

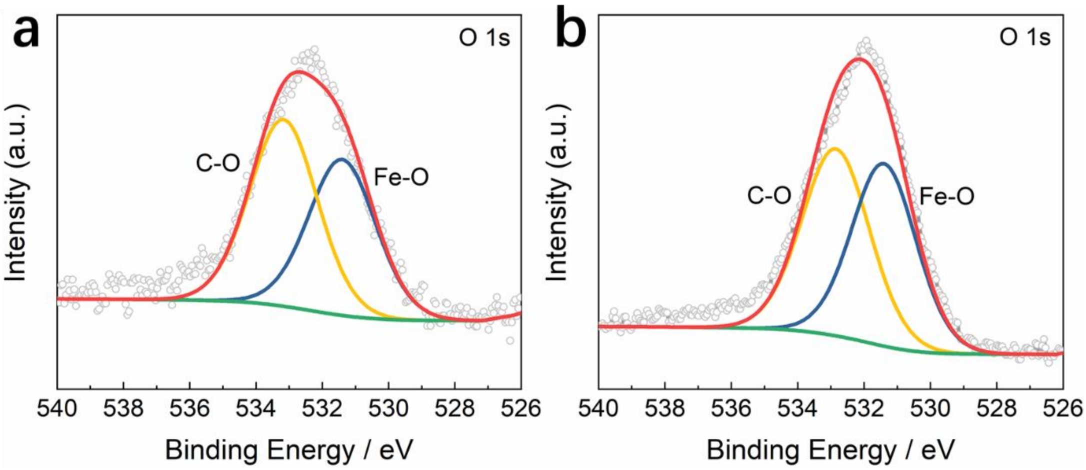

Figure S9. High resolution O 1s XPS for a) Fe/N-G-800 and b) Fe@Fe/N-G-800.

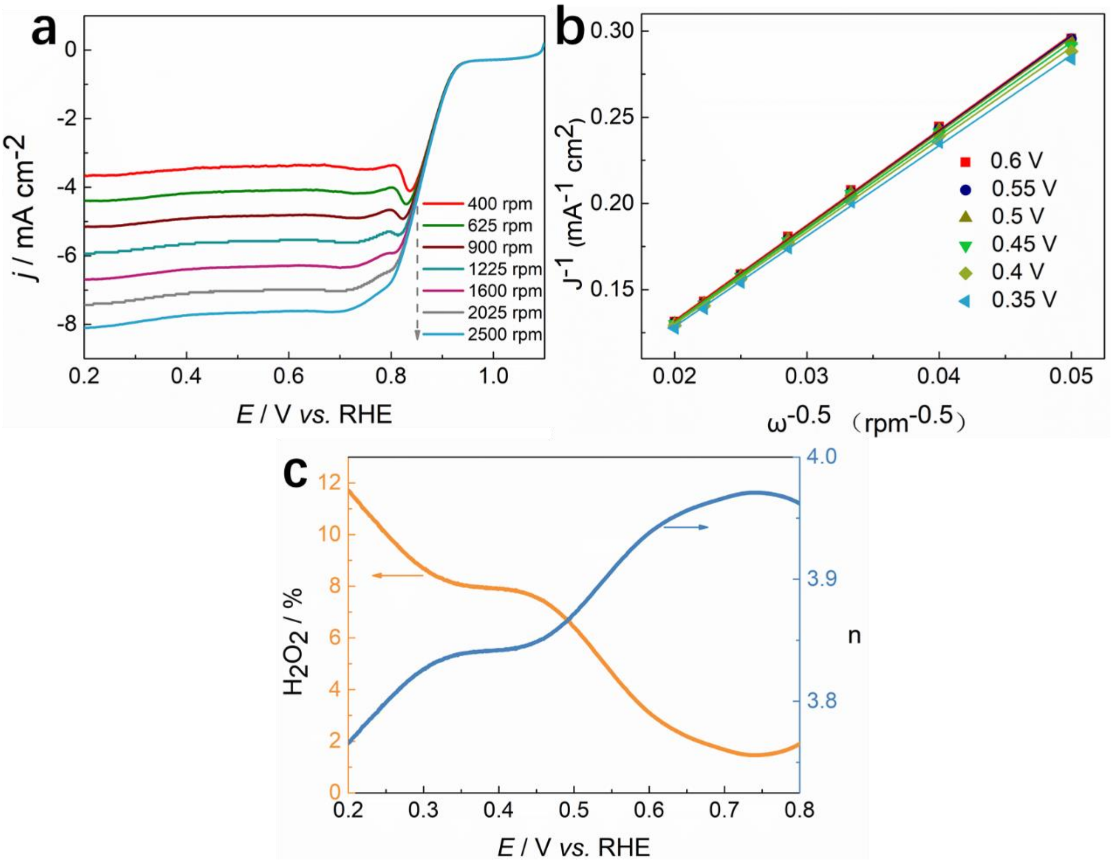

Figure S10. a) ORR polarization curves of Fe/N-G-800 at different rotating speeds; b) the corresponding K-L plots and c) hydrogen peroxide yield and corresponding electron transfer number during ORR process calculated using RRDE method.

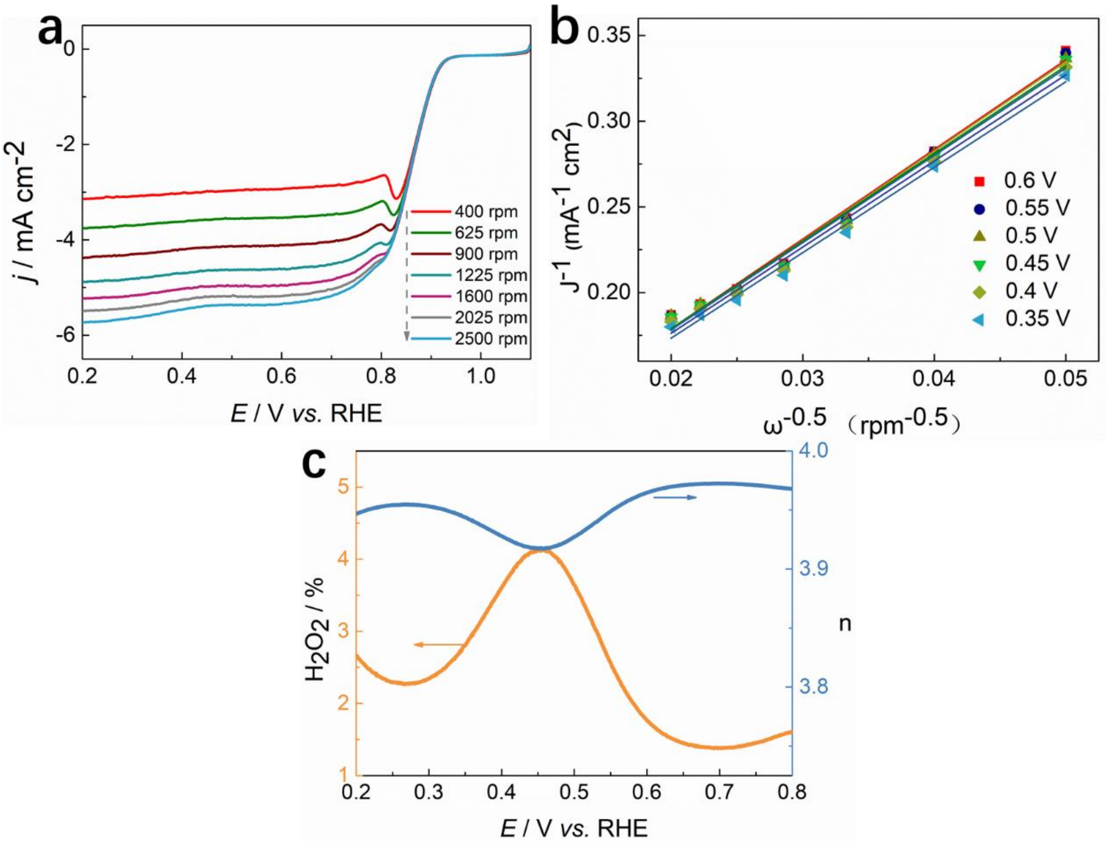

Figure S11. a) ORR polarization curves of Fe/N-G-800/FePc at different rotating speeds; b) the corresponding K-L plots and c) hydrogen peroxide yield and corresponding electron transfer number during ORR process calculated using RRDE method.

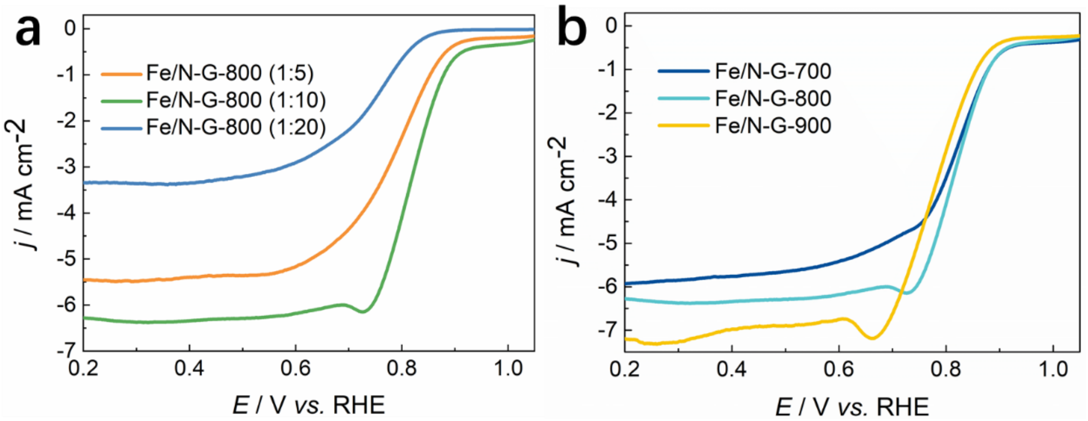

Figure S12. LSV curves of a) Fe/N-G-800 (1:X) with different initial mass ratio of DA/$FeCl_3$, and b) Fe/N-G-T with different annealing temperature.

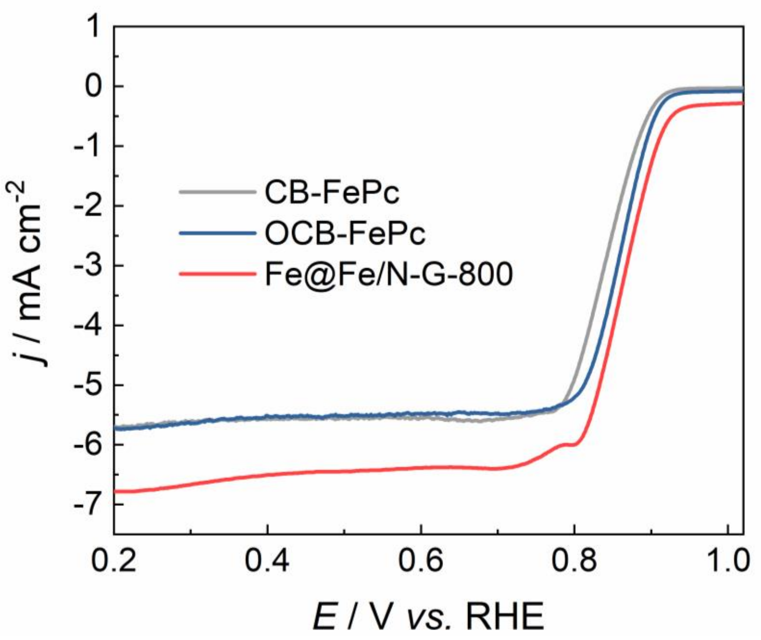

Figure S13. LSV curves of CB-FePc, OCB-FePc, and Fe@Fe/N-G-800.

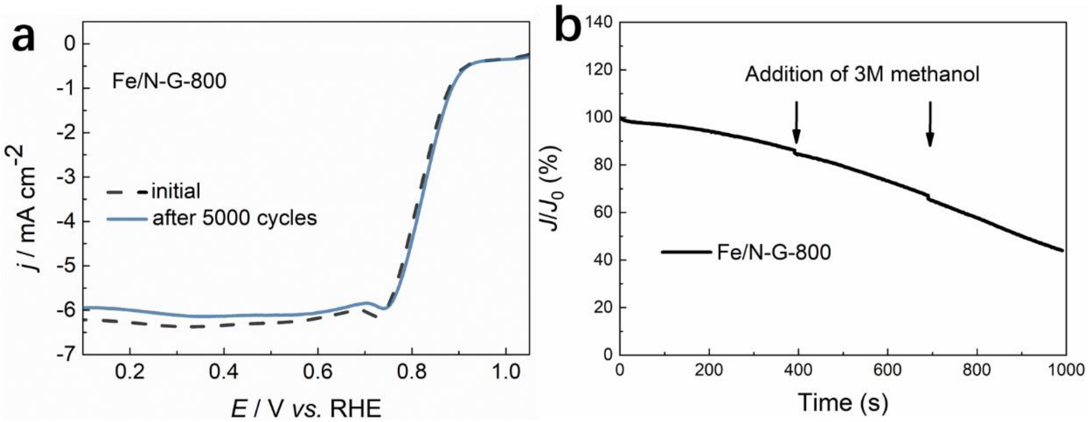

Figure S14. a) LSV curves of Fe/N-G-800 before and after cycling for 5000 cycles with 1600 rpm RDE; b) i–t CA responses for Fe/N-G-800 at 0.4 V and 1600 rpm with 3M methanol addition at around 400 s and 700 s. J_0 defines the initial current.

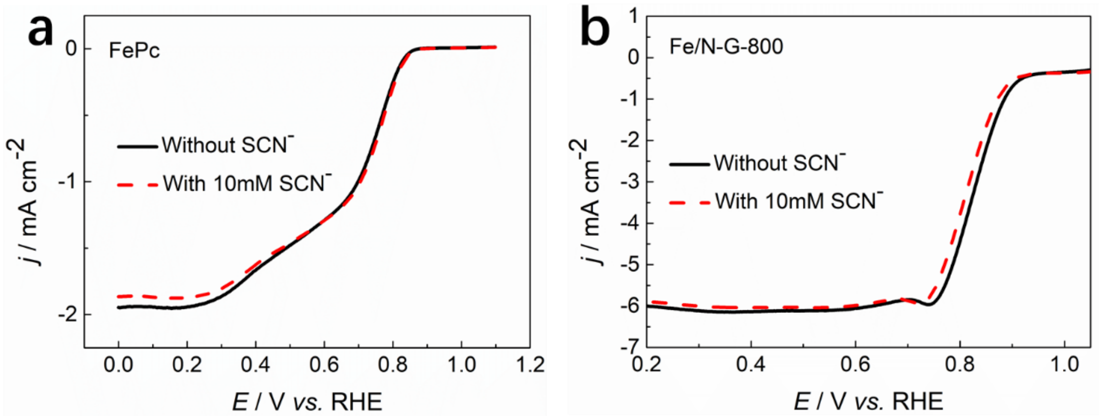

Figure S15. a) LSV curves of FePc and b) Fe/N-G-800 in 0.1 M KOH aqueous solution without (black) and with (red) 10 mM NaSCN.

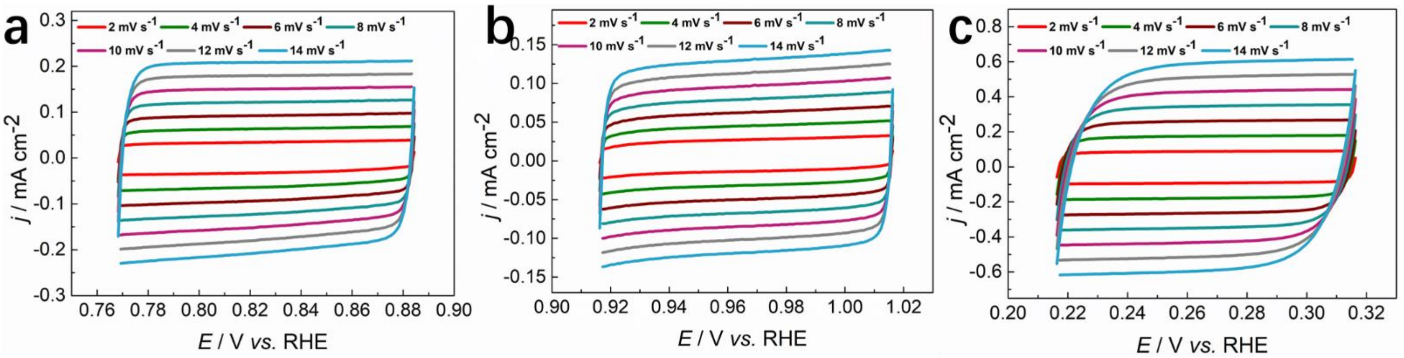

Figure S16. Cyclic voltammograms for a) Fe/N-G-800, b) Fe/N-G-800/FePc, and c) Fe@Fe/N-G-800 in the non-faradaic capacitance current range at scan rates of 2, 4, 6, 8, 10, 12 and 14 mV s^{-1}.

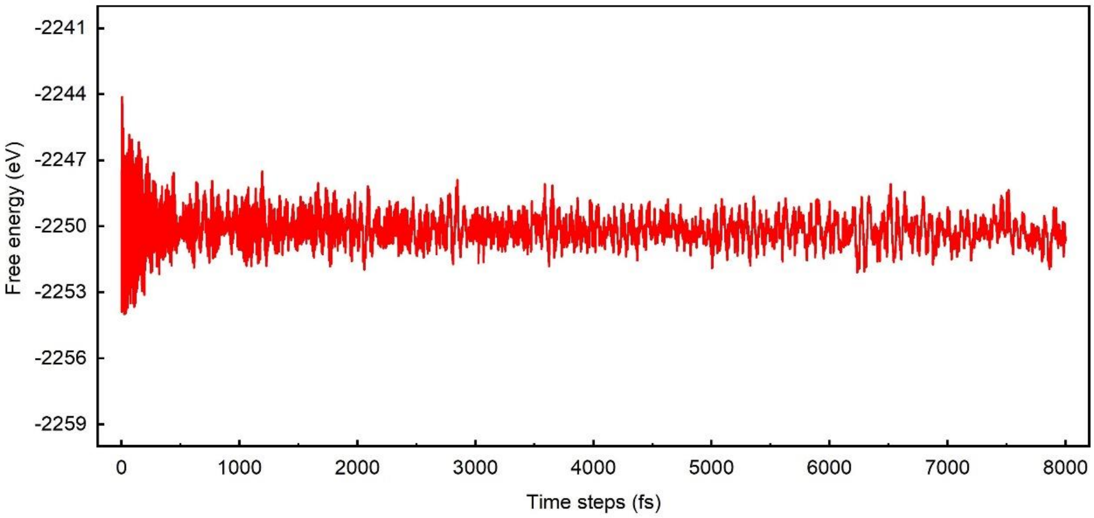

Figure S17. The evolution of free energy of Fe@Fe/N-G-800 versus simulation time of 8000 fs.

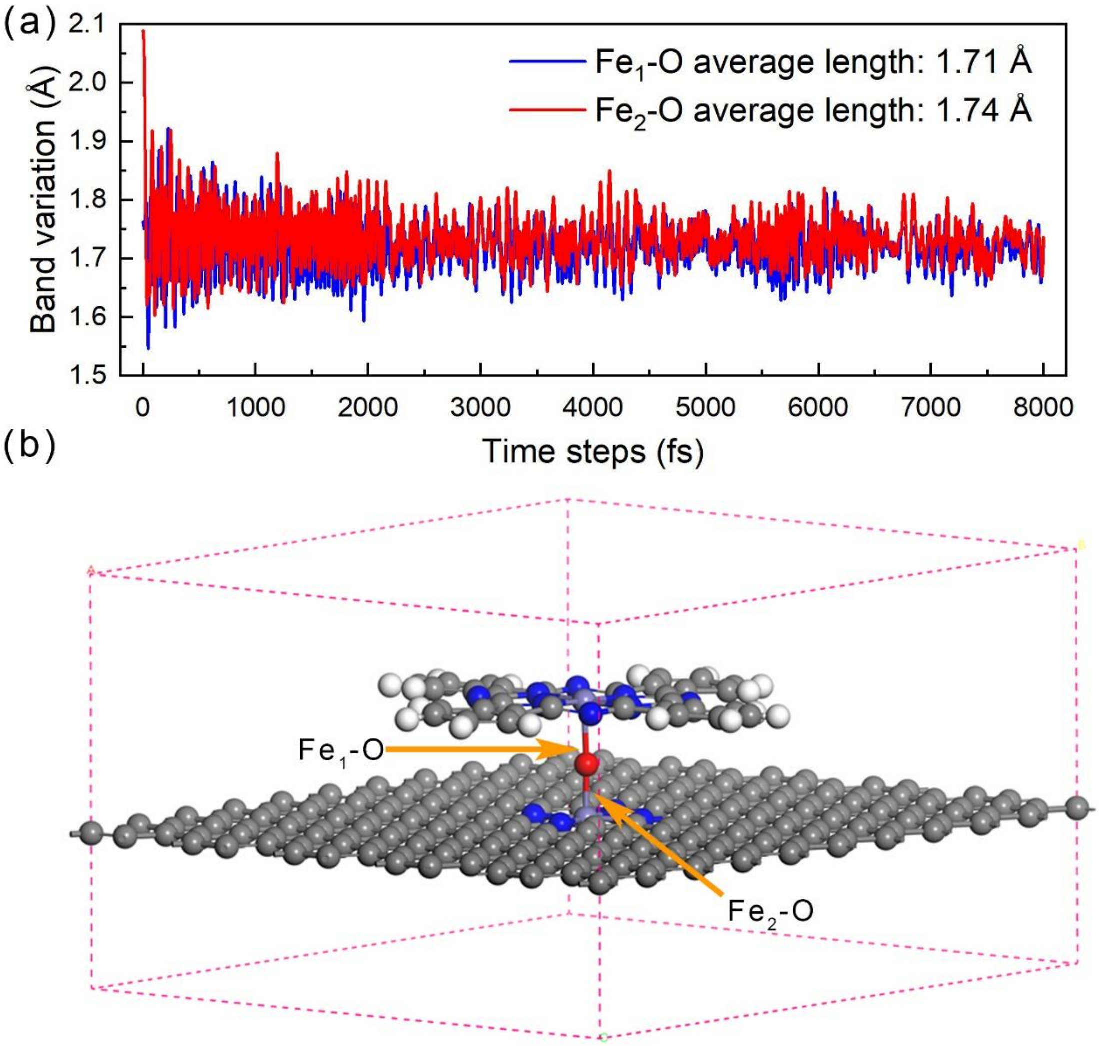

Figure S18. (a) Vibrations of the Fe_1-O and Fe_2-O bond lengths versus simulation time of 8000 fs for Fe@Fe/N-G-800. (b) The initial structure of Fe@Fe/N-G-800 and the location of Fe_1-O and Fe_2-O bonds.

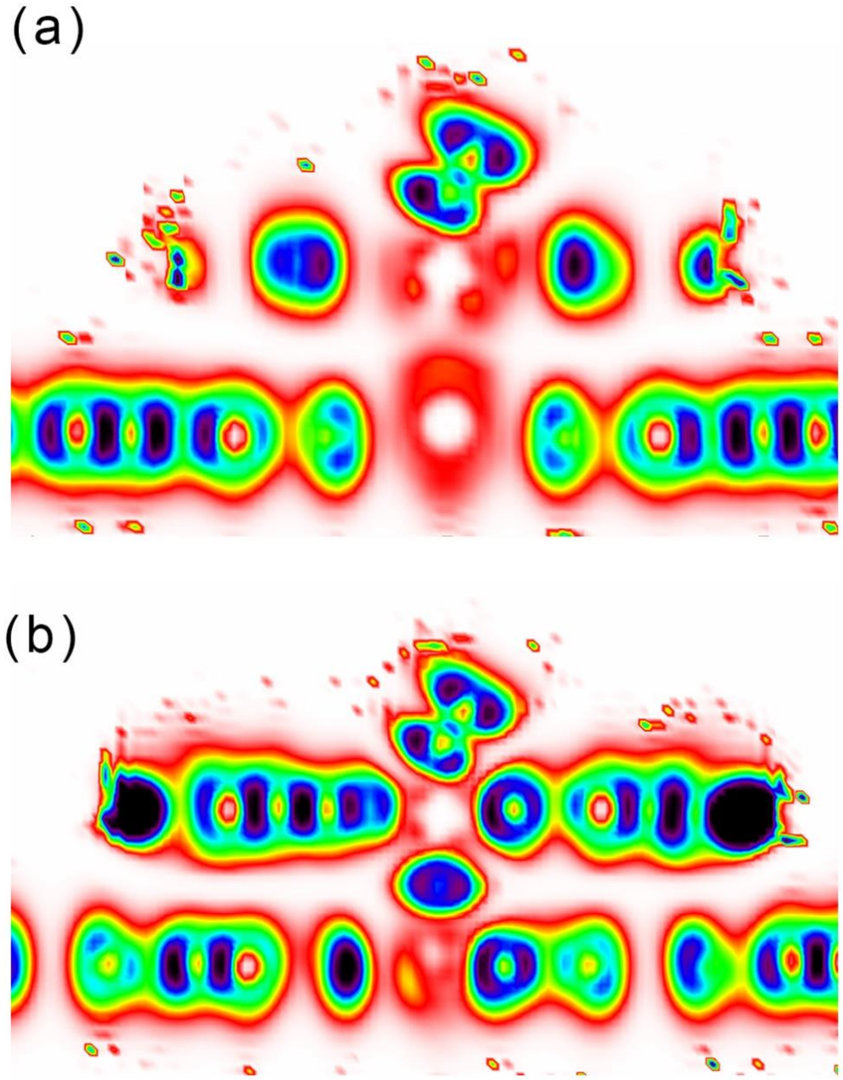

Figure S19. Electron localization functions of O_2 adsorbed (a) Fe/N-G-800/FePc and Fe@Fe/N-G-800.

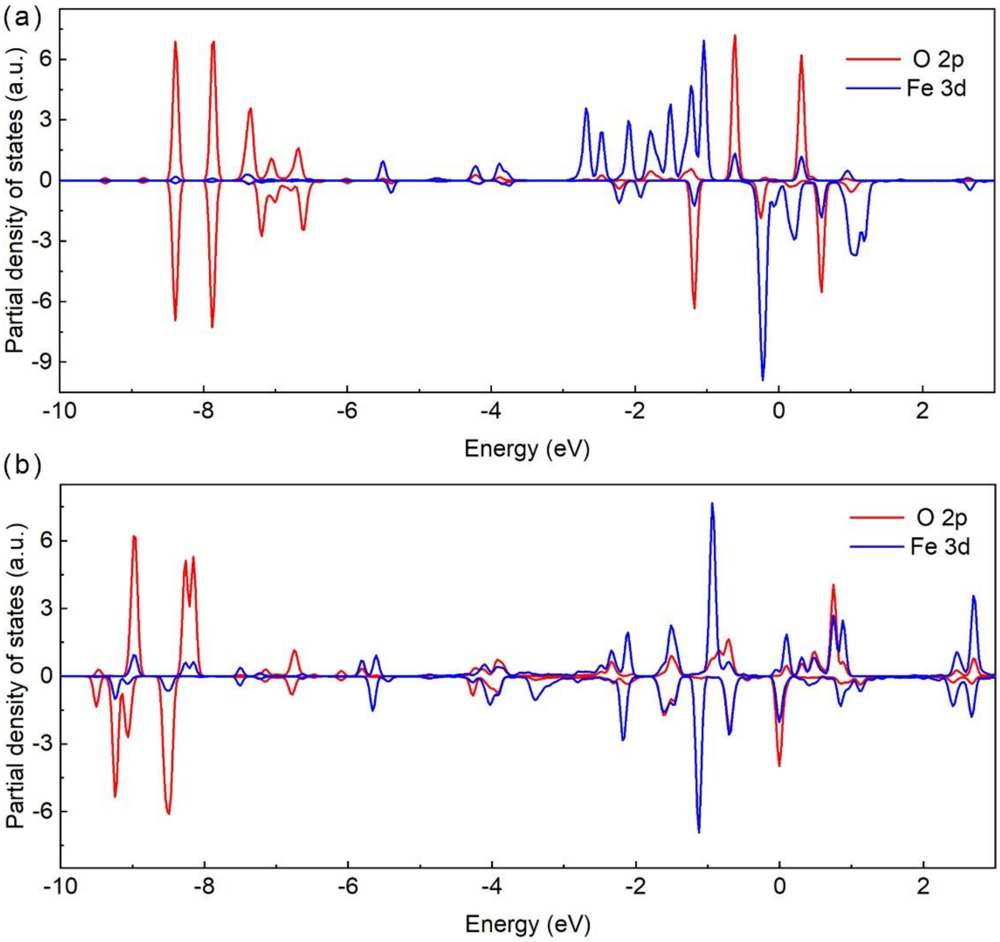

Figure S20. The partial density of states of O_2 adsorbed (a) Fe/N-G-800/FePc and (b) Fe@Fe/N-G-800**.**

Table S1. BET surfaces area, BJH desorption average pore size and BJH desorption pore volume for Fe/N-G-800 and Fe@Fe/N-G-800.

Samples	BET surfaces area / m^2 g^{-1}	Average Pore Size / nm	Pore Volume / cm^3 g^{-1}
Fe/N-G-800	970.5	3.6	0.49
Fe@Fe/N-G-800	988.9	3.8	0.65

Table S2. The element compositions and the ratios of various nitrogen-functionality in Fe/N-G-800 and Fe@Fe/N-G-800.

Samples	C content [at%]	N content [at%]	O content [at%]	Fe content [at%]	pyridinic-N ratio	graphitic-N ratio	oxidized-N ratio
Fe/N-G-800	95.09	2.50	2.18	0.23	27.8%	48.9%	23.3%
Fe@Fe/N-G-800	90.56	5.08	3.88	0.48	59.6%	29.9%	10.5%
Fe/N-G-800/FePc	91.36	3.41	4.62	0.61	51.7%	38.0%	10.3%

Table S3. EXAFS fitting results of Fe in Fe@Fe/N-G-800 and FePc.

Sample	Path	Coordination number	R(Å)	σ^2 (10^{-3} Å^2)	R factor
Fe/N-G-800	Fe-N	3.8±0.7	2.05±0.04	10.2	0.0109
	Fe-O	1.0±0.6	2.05±0.02	1.7	
	Fe-Fe	0.8±0.2	3.05±0.02	6.8	
Fe@Fe/N-G-800	Fe-N	4.30 ± 0.6	2.06 ± 0.02	2.2	0.0047
	Fe-O	1.2±0.3	1.89±0.04	1.5	
	Fe-Fe	1.3±0.3	2.44±0.02	14.3	
FePc	Fe-N	4.08 ± 0.4	1.93 ± 0.03	4.03	0.018
Fe foil	Fe-Fe	8	2.47±0.01	0.0049	0.0024
	Fe-Fe	6	2.86±0.01	0.0065	

R is the distance between absorber and backscatter atoms, σ^2 is Debye-Waller factor to account for both thermal and structural disorders, R factor indicates the goodness of the fit

Table S4. Summary of recently reported ORR performances of different non-precious metal catalysts under alkaline conditions (0.1 M KOH).

Catalysts	**Catalyst loading (μg cm^{-2})**	***E*$_{1/2}$ (V vs. RHE)**	***E*$_{1/2}$ of reported Pt/C (V vs. RHE)**	**Reference**
Fe@Fe/N-G-800	384	0.866	0.850	**This work**
Fe-N/P-C-700	600	0.867	0.848	J. Am. Chem. Soc. 2020, 2, 2404-2412
Ni-N_4/GHSs/Fe-N_4	255	0.830	0.860	Adv. Mater. 2020, 32, 2003134
Fe/OES	400	0.850	0.850	Angew. Chem. Int. Ed. 2020, 59, 7384 -7389
W_2N/WC	300	0.810	-	Adv. Mater. 2020, 32, 1905679
Fe_1-HNC-500-850	630	0.842	0.831	Adv. Mater. 2020, 32, 1906905
10Co-N@DCNF	100	0.830	0.840	Angew. Chem. Int. Ed. 2020, 59, 6122-6127
Gd_2O_3-Co/NG	255	0.820	-	Adv. Energy Mater. 2020, 1903833
Mo SACs/N-C	1620	0.830	0.900	Nano Energy 67 (2020) 104288
Co(mIm)–NC(1.0)	600	0.820	0.855	Nature Catalysis 3 (2020) 1044-1054
Fe–N–C/MXene	100	0.840	0.900	ACS Nano 2020, 14, 2436-2444
N-CoS_2 YSSs	500	0.810	0.850	Adv. Sci. 2020, 7, 2001178
Co-N_3C_1	400	0.824	-	ACS Catal. 2020, 10, 5862-5870

Reference

[1] Momma, K.; Izumi, F. Vesta 3for three-dimensional visualization of crystal, volumetric and morphology data. *Journal of Applied Crystallography* **2011,** *44*, 1272-1276.

[2] Lou, P.; Lee, J. Y. Gec/gan vdw heterojunctions: A promising photocatalyst for overall water splitting and solar energy conversion. *ACS Appl Mater Interfaces* **2020,** *12*, 14289-14297.

[3] Lee, J.; Huang, J.; Sumpter, B. G.; Yoon, M. Strain-engineered optoelectronic properties of 2d transition metal dichalcogenide lateral heterostructures. *2D Materials* **2017,** *4*, 021016.

[4] Li, J.; Zhang, S.; Wang, Y.; Duan, H. M.; Long, M. First-principles study of strain modulation in s3p2/black phosphorene vdw heterostructured nanosheets for flexible electronics. *ACS Applied Nano Materials* **2020,** *3*, 4407-4417.

[5] Zhang, W.; Zou, G.; Choi, J. H. Adsorption behavior of the hydroxyl radical and its effects on monolayer mos2. *ACS Omega* **2020,** *5*, 1982-1986.

[6] Pan, J.; Shao, X.; Xu, X.; Zhong, J.; Hu, J.; Ma, L. Organic dye molecules sensitization-enhanced photocatalytic water-splitting activity of mos2 from first-principles calculations. *The Journal of Physical Chemistry C* **2020,** *124*, 6580-6587.

[7] Zhou, Z.; Zhang, Y.; Zhang, X.; Niu, X.; Wu, G.; Wang, J. Suppressing photoexcited electron–hole recombination in mose2/wse2 lateral heterostructures via interface-coupled state engineering: A time-domain ab initio study. *Journal of Materials Chemistry A* **2020,** *8*, 20621-20628.

[8] Grimme, S. Semiempirical gga-type density functional constructed with a long-range dispersion correction. *J Comput Chem* **2006,** *27*, 1787-99.

[9] Ataca, C.; Şahin, H.; Ciraci, S. Stable, single-layer mx2 transition-metal oxides and dichalcogenides in a honeycomb-like structure. *The Journal of Physical Chemistry C* **2012,** *116*, 8983-8999.

[10] Han, S. W.; Kwon, H.; Kim, S. K.; Ryu, S.; Yun, W. S.; Kim, D. H.; Hwang, J. H.; Kang, J. S.; Baik, J.; Shin, H. J. et al. Band-gap transition induced by interlayer van der waals interaction in mos2. *Physical Review B* **2011,** *84*.

[11] Nørskov, J. K.; Rossmeisl, J.; Logadottir, A.; Lindqvist, L.; Kitchin, J. R.; Bligaard, T.; Jónsson, H. Origin of the overpotential for oxygen reduction at a fuel-cell cathode. *Journal of Physical Chemistry B* **2004,** *108*, 17886-17892.

[12] Zhang, T.; Anderson, A. B. Oxygen reduction on platinum electrodes in base: Theoretical study. *Electrochimica Acta* **2007,** *53*, 982-989.

[13] Zitolo, A.; Goellner, V.; Armel, V.; Sougrati, M. T.; Mineva, T.; Stievano, L.; Fonda, E.; Jaouen, F. Identification of catalytic sites for oxygen reduction in iron- and nitrogen-doped graphene materials. *Nat Mater* **2015,** *14*, 937-42.

[14] Yuan, K.; Lutzenkirchen-Hecht, D.; Li, L.; Shuai, L.; Li, Y.; Cao, R.; Qiu, M.; Zhuang, X.; Leung, M. K. H.; Chen, Y. et al. Boosting oxygen reduction of single iron active sites via geometric and electronic engineering: Nitrogen and phosphorus dual coordination. *J Am Chem Soc* **2020,** *142*, 2404-2412.